

Article

Not peer-reviewed version

Effect of Roller Burnishing and Slide Roller Burnishing on Surface Integrity of AISI 316 Steel: Theoretical and Experimental Comparative Analysis

[Jordan Maximov](#)*, [Galya Duncheva](#), [Angel Anchev](#), [Vladimir Dunchev](#), Kalin Anastasov, Petya Daskalova

Posted Date: 13 December 2023

doi: 10.20944/preprints202312.0975.v1

Keywords: austenitic stainless steel; surface integrity; roller burnishing; slide roller burnishing



Preprints.org is a free multidiscipline platform providing preprint service that is dedicated to making early versions of research outputs permanently available and citable. Preprints posted at Preprints.org appear in Web of Science, Crossref, Google Scholar, Scilit, Europe PMC.

Copyright: This is an open access article distributed under the Creative Commons Attribution License which permits unrestricted use, distribution, and reproduction in any medium, provided the original work is properly cited.

Article

Effect of Roller Burnishing and Slide Roller Burnishing on Surface Integrity of AISI 316 Steel: Theoretical and Experimental Comparative Analysis

Jordan Maximov ^{1,*}, Galya Duncheva ¹, Angel Anchev ¹, Vladimir Dunchev ¹, Kalin Anastasov ² and Petya Daskalova ³

¹ Department of Material Science and Mechanics of Materials, Technical University of Gabrovo, 5300 Gabrovo, Bulgaria; duncheva@tugab.bg (G.D.); anchev@tugab.bg (A.A.); v.dunchev@tugab.bg (V.D.)

² Department of Mechanical Engineering Equipment and Technologies, Technical University of Gabrovo, 5300 Gabrovo, Bulgaria; kalinanastasov@abv.bg (K.A.)

³ Department of Industrial Design and Textile Engineering, Technical University of Gabrovo, 5300 Gabrovo, Bulgaria; p.daskalova@abv.bg (P.D.)

* Correspondence: jordanmaximov@gmail.com

Abstract: The article presents a new method called slide roller burnishing (SRB) for cold working of cylindrical surfaces on machine tools, implemented with a novel multi-functional device. The machined material was chromium–nickel austenitic stainless steel. The deforming element is a toroidal roller whose axis crosses that of the workpiece. As a result, a relative sliding velocity occurs in the contact zone between the roller and the machined surface. The sliding velocity vector is set using the burnishing device. The theoretical background of SRB is presented. When the two axes are parallel, the well-known roller burnishing (RB) method is implemented. Thus, RB is a special case of SRB. Both processes are realized using the multi-functional burnishing device. The RB process was studied experimentally and optimized according to three criteria, based on the relationship between the surface integrity and operating behavior of the respective component, to achieve three processes: smoothing, hardening and mixed burnishing. Using the optimal RB parameters obtained, the dependence of the results of SRB on the crossing angle was investigated and optimized. A comparative analysis was performed between the optimized RB and SRB processes (respectively for their three variants: smoothing, hardening and mixed) based on geometrical and physical–mechanical characteristics of the surface integrity. The main advantage of the SRB is that it provides smaller height roughness parameters and a higher surface microhardness than RB.

Keywords: austenitic stainless steel; surface integrity; roller burnishing; slide roller burnishing

1. Introduction

One of the methods used for finishing processing of metal components is static surface cold working (SCW), based on plastic deformation of the surface and near-subsurface layers. SCW reduces the height parameters of roughness, increases the surface microhardness, and introduces compressive residual stresses (RSs) at a depth of approximately 0.8mm [1]. Any method implementing static SCW is a type of burnishing method and includes one or more deforming elements that perform a relative movement toward the machined surface and have a hardness much greater than that of the surface [2]. According to the type of contact between the deforming element and the treated surface, burnishing methods fall into two groups: with sliding friction contact or with rolling contact. The slide burnishing (SB) method is implemented via sliding contact, while roller burnishing (RB) and ball burnishing (BB) are implemented via rolling contact (Figure 1). The deforming elements for RB and BB are, respectively, rollers (the working surface is usually cylindrical, barrel-shaped, or toroidal) and balls. Both methods implement one of two processes: roller burnishing or deep rolling, according to the Ecoroll classification [1]. The aim of the former process is a strong reduction of the height parameters to achieve a mirror-like surface. The latter process aims primarily at maximum strain hardening, resulting in maximum surface microhardness

and maximum compressive RS distributed to maximum depth from the surface layer. The choice of process (roller burnishing or deep rolling) depends on the desired operational behavior of the respective metal component in accordance with the known relationship between the finishing, the surface integrity, and the operating behavior [3]. The SB method, depending on the processed material and the purpose of the corresponding metal component, can also implement different processes: smoothing, hardening, or mixed [4].

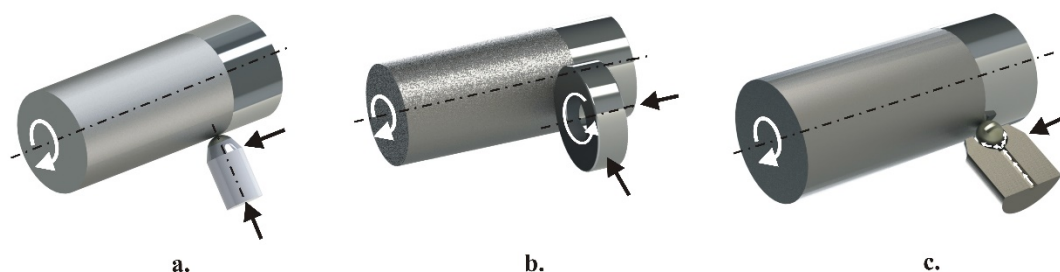


Figure 1. Burnishing methods: a. slide burnishing; b. roller burnishing; c. ball burnishing.

Few studies have focused on comparing of SB, RB, and BB, according to the criteria of surface integrity characteristics and operational behavior of components processed using these methods. An extensive study and comparison of SB (implemented with a spherical-ended diamond insert) with RB and deep rolling processes was carried out in [5], in which they were used to process unhardened 41Cr4 steel. It was found that SB (with a burnishing force of 300 N) achieves lower roughness, higher surface microhardness and higher fatigue strength at room temperature than RB (300 N) and deep rolling (1300 N) processes at equal governing factors (except for burnishing force). Due to sliding friction contact, SB achieves greater equivalent plastic deformation of the surface and near-subsurface layers, which causes greater strain hardening. As a result, the surface microhardness and introduced compressive RS (in absolute value) are greater, leading to greater (low-, high-, and mega-cycle) fatigue strength. However, these beneficial effects of SB are most pronounced for unhardened steel components operating under normal service conditions. At high temperatures, RS relaxation is decisive. For example, in an AISI 304 steel component, the compressive RS (measured for both the austenitic and martensitic phases due to the presence of strain-induced α' -martensite) introduced by SB with a spherical ended diamond insert is reduced from 50% to 0% from the surface layer to a depth of up to 0.1mm after heating at a temperature of 450°C for two hours [6]. At greater depth, the RS distribution remains nearly constant. To increase the fatigue life of hardened steel components operating at high temperatures, low-plasticity burnishing (LPB) with dynamic adaptive control was developed [7]. The LPB process is implemented using the BB method with a hydrostatic sphere, but the equivalent plastic strain of the surface layer is kept below 5%. Thus, the introduced RS remains stable even at a temperature of 600°C [8,9]. However, the present study focuses on the burnishing of components operating at normal temperatures and in particular, chromium-nickel austenitic stainless steel operating at a temperature below 350°C, given the propensity of these steels to intergranular corrosion, as well as the so-called "brittleness at 475°C" [10].

Numerous authors have conducted extensive research on using conventional burnishing technologies to improve the surface integrity and operating behavior of chromium-nickel austenitic stainless steels. For instance, RB was employed to improve the surface integrity and wear resistance of 316L steel components [11], and to finish the surfaces of holes in 304 steel [12]. Improvement of the corrosion behavior of 304L steel by a hybrid process (RB and cryogenic cooling) was demonstrated in [13]. The effects of BB with a hydrostatic sphere, implemented with a deep rolling process, on the fatigue behavior of 304 steel specimens were studied in [14–19]. Nanostructuring BB with a hydrostatic ball of 316L steel was implemented in [20]. BB with a hydrostatic sphere was applied in [21] to improve the wear resistance of 316L steel. Improvement of the surface integrity of 317 and 321 steel components via SB was demonstrated in [22–25]. The effect of SB on the fatigue strength of 304 steel was investigated in [6].

In the conventional RB method, the motion of the deforming roller relative to the machined surface is a superposition of pure rolling and rectilinear translation parallel to the workpiece axis. Thus, the contact spot (between the deforming element and workpiece) moves along a helical line described on the surface being burnished. The angle of inclination of the screw line depends only on the diameter of the workpiece and the feed rate. Similarly, in the SB method, the tip of the deforming diamond (or other hard material) insert moves in a helical line along the treated surface. The kinematics of both methods (RB and SB) greatly limit their ability to create different surface textures. However, if the axis of the deforming roller with a toroidal working surface crosses the workpiece axis, a relative sliding velocity will occur between the roller and the machined surface. The magnitude and direction of this velocity can be varied widely by adjusting the crossing angle. Thus, SB is implemented instead of the familiar RB method. The new method is called slide roller burnishing (SRB). The present study provides a theoretical and experimental comparison of RB and SRB processes. The objects of comparison are the main characteristics (roughness, microhardness, and RS) of the surface integrity of processed AISI 316 steel cylindrical samples. Figure 2 shows a flow chart of the investigations.

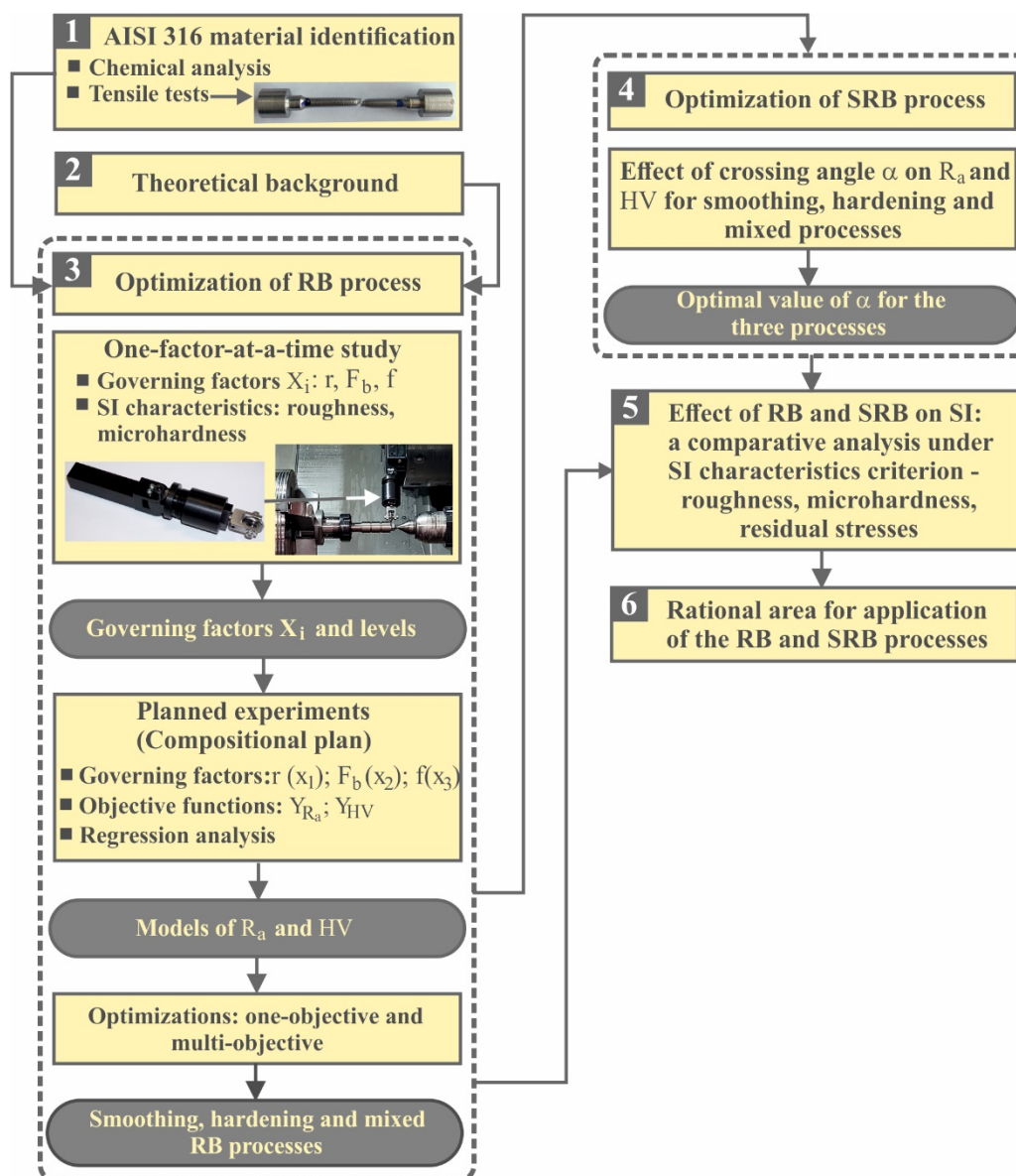


Figure 2. Flow chart of the investigations.

2. Theoretical Background

2.1. Implementation of SRB

The implementation of the SRB process on a lathe is shown in Figure 3. The workpiece, driven by the machine spindle, rotates about its own axis with an angular velocity $\vec{\omega}_w$. The deforming toroidal roller is pressed against the workpiece with a force (the burnishing force) in a direction perpendicular to the axis of the workpiece. The axis of the deforming roller crosses the axis of the workpiece at an angle α , such that $0^\circ < |\alpha| < 90^\circ$ (see Figure 4). As a result of the contact between the roller and the machined surface, the roller rotates around its own axis with an angular velocity $\vec{\omega}_r$. The feed movement is carried out by the roller, which moves translationally, parallel to the axis of the workpiece.

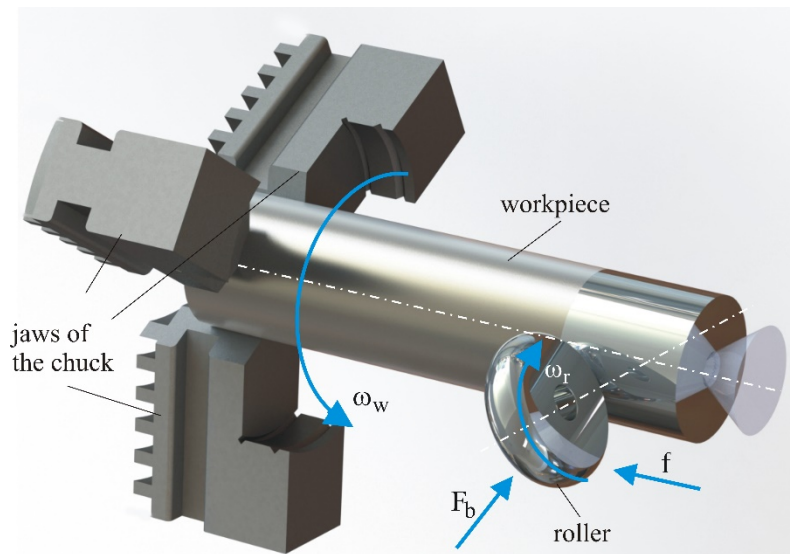


Figure 3. Implementation of slide roller burnishing – general view.

2.2. Kinematics of the Main Motion of SRB

The kinematics of the main motion of the SRB method (when the feed motion is turned off) are shown schematically in Figure 4a. Point O is the center of contact between the deforming roller (r) and the workpiece (w). The velocity of point O, considered as a point on the periphery of the workpiece, has magnitude

$$v_{O,w} = \omega_w r_w, \quad (1)$$

where r_w is the workpiece radius. The magnitude of the velocity of point O, considered as a point on the equatorial circle of the toroidal surface of the roll, is

$$v_{O,r} = \omega_r r_r, \quad (2)$$

where r_r is the radius of the equatorial circle. The relationship between the magnitudes of the two velocities is

$$v_{O,r} = v_{O,w} \cos \alpha. \quad (3)$$

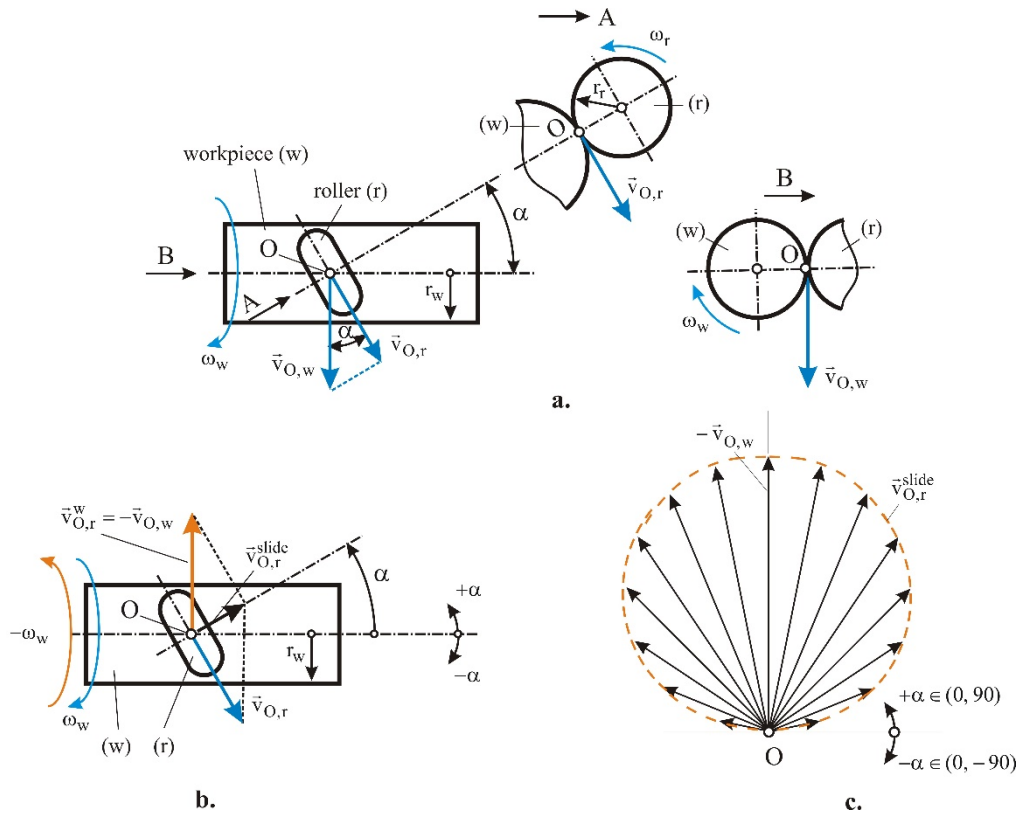


Figure 4. Kinematics of SRB (feed motion is turned off): a. absolute motions; b. relative motion of the deforming roller to the workpiece; c. diagram of the unit-normalized sliding velocity vector.

If an angular velocity $-\bar{\omega}_w$ is imparted to the deforming roll–workpiece system (Figure 4b), the workpiece will be stationary and the deforming roller will rotate about the axis of the workpiece with an angular velocity $-\bar{\omega}_w$, whereby it will simultaneously rotate about its own axis with an angular velocity $\bar{\omega}_r$. Then the velocity of point O belonging to the deforming roller is a vector sum of two components:

$$\vec{v}_{O,r}^{\text{slide}} = -\vec{v}_{O,w} + \vec{v}_{O,r}, \quad (4)$$

The resulting vector $\vec{v}_{O,r}^{\text{slide}}$ is the sliding velocity of the roller relative to the workpiece. From the velocity triangle (Figure 3b) it follows for the magnitude of the sliding velocity that

$$v_{O,r}^{\text{slide}} = v_{O,w} \sin \alpha. \quad (5)$$

The slide velocity magnitude diagram is shown in Figure 4c. When $\alpha = 0^\circ$, the axes of the workpiece and the roller are parallel. The roller performs clean rolling (without slipping) with respect to the machined surface of the workpiece, i.e., the method implemented is RB. When $\alpha = \pm 90^\circ$, the workpiece and roll axes are orthogonally crossed, the roller is stationary, and the sliding velocity is maximal in magnitude: it is equal to the speed of a peripheral point of the workpiece. In this case, the SB method is performed. For all other cases ($0^\circ < |\alpha| < 90^\circ$), the SRB method is implemented. Therefore, the RB and SB method are both special cases of the SRB method.

2.3. Kinematics of SRB with Feed Motion Included

The kinematics of the SRB method with feed motion included are shown schematically in Figure 5.

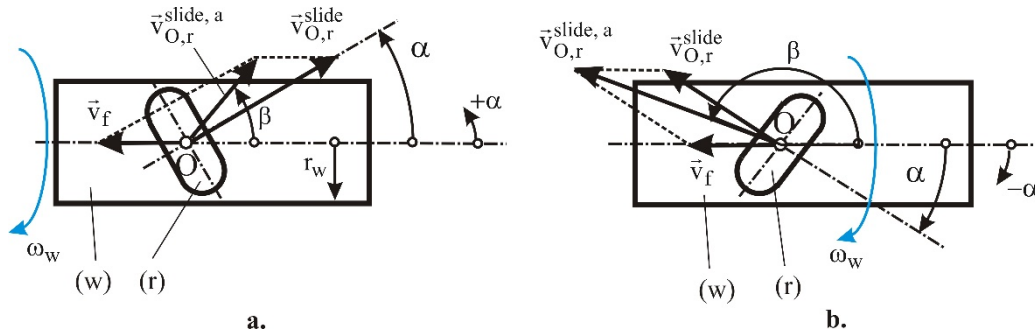


Figure 5. Kinematics of SRB (feed motion is turned on): a. $0^\circ < \alpha < 90^\circ$; b. $-90^\circ < \alpha < 0^\circ$.

The velocity \vec{v}_f of the roller during the feed motion has a magnitude

$$v_f = nf, \quad (6)$$

where n is the frequency of rotation of the workpiece (the number of revolutions per unit time) and f is the feed rate (the displacement per revolution). The absolute sliding velocity $\vec{v}_{O,r}^{\text{slide},a}$ is the vector sum

$$\vec{v}_{O,r}^{\text{slide},a} = \vec{v}_{O,r}^{\text{slide}} + \vec{v}_f. \quad (7)$$

For brevity, the sliding velocities $\vec{v}_{O,r}^{\text{slide}}$ and $\vec{v}_{O,r}^{\text{slide},a}$ are denoted by \vec{v} and \vec{v}^a , respectively. For their magnitudes, it follows that

$$v_{O,r}^{\text{slide}} = v, \quad (8)$$

$$v_{O,r}^{\text{slide},a} = v^a. \quad (9)$$

Taking into account (5), (8), and (9), and the geometrical dependences shown in Figure 4, for the magnitude of the absolute sliding velocity it follows that

$$v^a = \sqrt{v_{O,w}^2 \sin^2 \alpha + v_f^2 - v_{O,w} v_f \sin 2\alpha}. \quad (10)$$

It is appropriate to normalize v and v^a to unity:

$$v_n = \frac{v}{v_{O,w}} = \sin \alpha, \quad (11)$$

$$v_n^a = \frac{v^a}{v_{O,w}} = \sqrt{\sin^2 \alpha - k_v \sin 2\alpha + k_v^2}, \quad (12)$$

where (taking into account that $\omega_w = \frac{\pi n}{30}$)

$$k_v = \frac{v_f}{v_{O,w}} = \frac{30f}{\pi r_w}. \quad (13)$$

The angle β between the absolute sliding velocity vector \vec{v}^a and the workpiece axis is:

$$\beta = \arccos \frac{v \cos \alpha - v_f}{v^a} = \arccos \frac{\sin \alpha \cos \alpha - k_v}{\sqrt{\sin^2 \alpha - k_v \sin 2\alpha + k_v^2}}. \quad (14)$$

Figure 6 shows the change in the magnitudes of the absolute sliding velocity \vec{v}^a and sliding velocity \vec{v} depending on the crossing angle α when $f = 0.1 \text{ mm/rev}$ and $r_w = 9.55 \text{ mm}$. The following conclusion can be drawn: excluding the small crossing angles ($0 < \alpha \leq 5^\circ$), the feed motion has little effect on the magnitude and direction of the sliding velocity \vec{v} , i.e., the absolute sliding velocity \vec{v}^a is not significantly different from the sliding velocity \vec{v} . The difference decreases with decreasing feed f and workpiece radius r_w ; see (11)–(13).

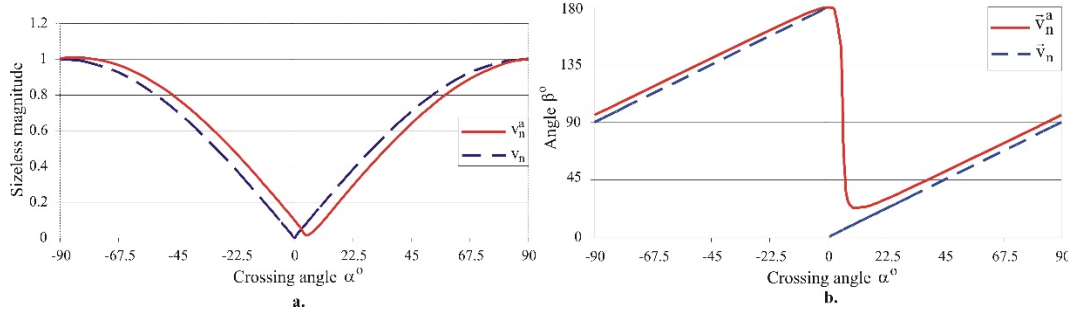


Figure 6. Variation of the characteristics of the absolute sliding velocity depending on the crossing angle α : a. magnitude normalized to unity; b. angle β .

It should be noted that in the known implementations of SB (with spherical- or cylindrical-ended diamond or another material), the sliding velocity \vec{v} is always perpendicular to the workpiece axis, which limits the range of surface textures that can be obtained. In contrast to SB, SRB allows the variation of the angle β within a wide range, and hence a greater variety of surface textures.

2.4. Theoretical Roughness

The so-called kinematic (theoretical) surface roughness depth $R_{z,\text{theor}}$ is defined based on two consecutive positions of the deforming roller for one complete rotation of the workpiece around its axis (Figure 7). The distance, measured along the axis of the workpiece, between the two positions of the roll is numerically equal to the feed rate f . The theoretical surface roughness depth at the RB process is

$$R_{z,\text{theor,RB}} \approx \frac{f^2}{8r}. \quad (15)$$

where r is the radius of the working toroidal surface of the deforming roller and f is the feed rate.

When the axes of the deforming roller and the workpiece are crossed, the section of the working toroidal surface of the deforming roller with a plane containing the axis of the workpiece is, to a first approximation, an ellipse with a major semi-axis $a = \frac{r}{\cos \alpha}$ and a minor semi-axis $b = r$. Then, the theoretical surface roughness depth for the SRB process is:

$$R_{z,\text{theor,SRB}} \approx \frac{(f \cos \alpha)^2}{8r}. \quad (16)$$

Comparing (15) and (16) shows that, for the same magnitudes of the governing factors of the two processes and the same roller geometry, SRB achieves smaller integral roughness height parameters.

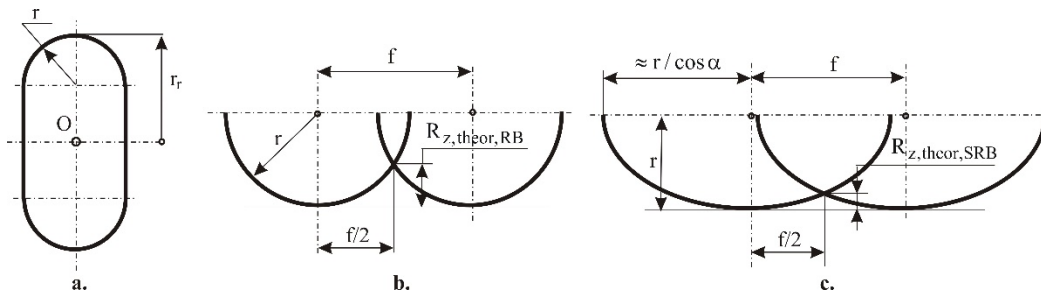


Figure 7. Visualization of the theoretical surface roughness depth: a. roller geometry; b. RB process; c. SRB process.

3. Experimental Conditions

3.1. Material

AISI 316 chromium–nickel austenitic stainless steel was obtained in the form of rolled bars with a diameter of 30 mm. The material was used in the as-received state. The chemical composition in weight percentages was established via optical emission spectrometer. Tensile tests at room temperature were conducted with a Zwick/Roell Vibrophore 100 testing machine using three specimens. The hardness was established with a ZWICK/Indentec–ZHV μ -S tester. Spherical-ended indenter with diameter of 2.5 mm, loading of 63 kg, and holding time of 10 s is used.

3.2. Burnishing Methods Implementation

RB and SRB were implemented on an Index Traub CNC lathe using a multifunctional burnishing device, as shown in Figure 8. All deforming rollers had the same radii on their equatorial circles: $r_r = 13$ mm (see Figure 7). Each specimen had an outer diameter of 30 mm, a thickness of 25 mm, and a central hole of 14 mm diameter. A group of specimens was positioned and fixed on a cylindrical mandrel (Figure 9). Each package was clamped to one side into the chuck and supported on the other side. Turning and burnishing were carried out in a single clamping process for the purposes of 1) minimizing the concentric run-out in burnishing, and 2) ensuring the same initial roughness (before burnishing) of all samples in the group. The governing factors were the radius r (see Figure 7) of the working toroidal surface of the deforming roller, the burnishing force F_b , and the feed rate f . RB and SRB were implemented using Vasco 6000 lubricant. The one-factor-at-a-time method and the planned experiment were conducted sequentially.

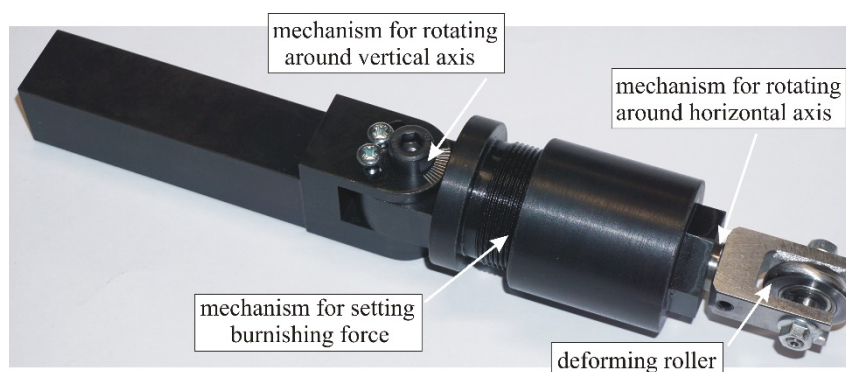


Figure 8. Burnishing device.

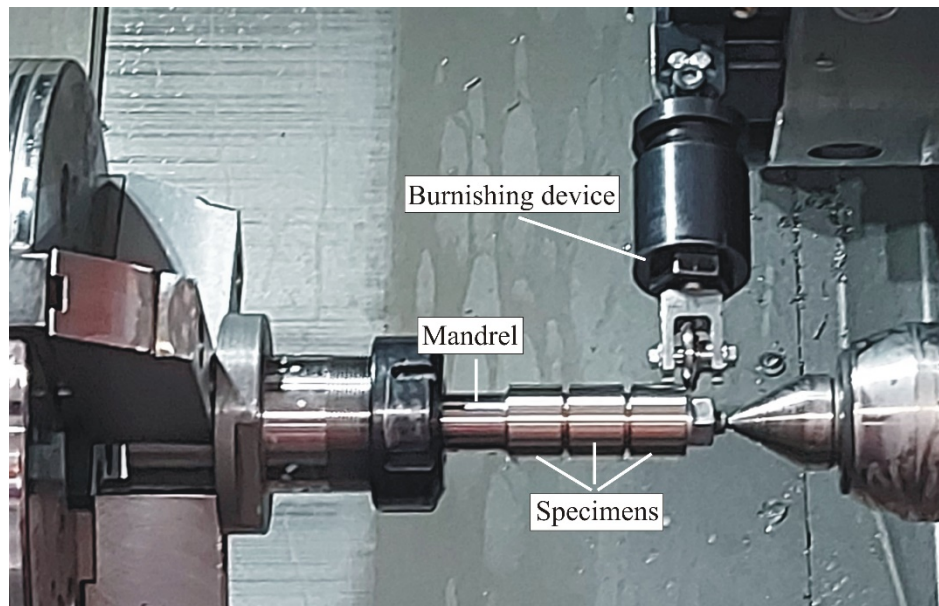


Figure 9. RB process implementation on Index Traub CNC lathe.

3.3. Measurement of Surface Integrity Characteristics

The roughness parameters were measured using a Mitutoyo SurfTest SJ-210 surface roughness tester. The roughness parameters were obtained as average values from measurements of six equally spaced specimen generatrices. A ZHV μ Zwick/Roell microhardness tester was used to measure the surface microhardness. The measurement conditions were a 10s holding time and 0.1 kgf loading. Twelve measurements were conducted for each specimen. The final surface microhardness magnitude for each specimen was the center of clustering of the twelve measurements. The RS distribution was measured with a Bruker D8 Advance X-ray diffractometer using the $\sin^2 \psi$ method and a least-squares fitting procedure. More detailed information on the measurement is provided in Table 1.

Table 1. Characteristics of the residual stress X-ray measurement.

Measuring device	Bruker D8 Advance diffractometer
X-ray tube	Long focus Cr – K α
Crystallographic plane	Fe(γ) - (220)
Diffraction angle (2θ)	128.78° (124° - 133°)
Measuring method	Offset coupled TwoTheta/Theta ($\sin^2 \psi$ method)
Scan mode	Continuous PSD fast
X-ray detector	SSD160-2 (1D scanning)
Collimator spot size	Standard Φ 1.0 mm
Measurement time for single scan	Approx. 35 s
Elastic constant s_1	-1.352E-6
Elastic constant $1/2s_2$	6.182E-6
Voltage	30 kV
Current	40 mA
Step size	0.5°
Time for step	1 s

4. Experimental Results and Discussion

4.1. Material Characteristics

The chemical composition of the AISI 316 steel used in this work is shown in Table 2. The remaining chemical elements (with a total content of 0.0382wt%) are Zr, Se, B, Sn, Pb, and Al. The specimen geometry and tensile tests results ($\sigma - \varepsilon$ diagram and main mechanical characteristics) are shown in Figure 10. The measured hardness was 215HB.

Table 2. Chemical composition (in wt%) of the tested AISI 316 austenitic stainless steel.

Fe	C	Si	Mn	P	S	Cr	Ni	Nb	Ti	Mo	Cu	Co	W	V
67.3	0.0384	0.169	1.75	0.0354	0.008	18.3	9.35	0.0358	0.0052	2.03	0.559	0.203	0.018	0.078

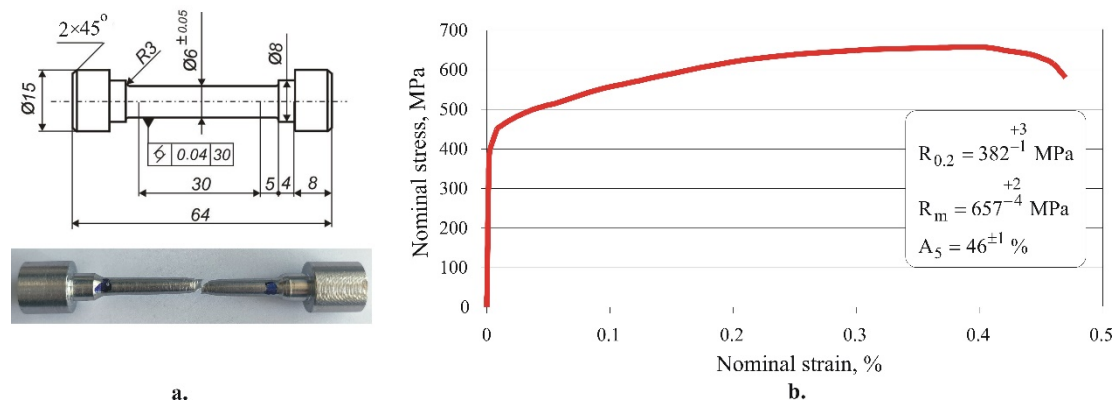


Figure 10. Tensile test outcomes: specimen geometry and photo; b. nominal stress–nominal strain diagram and main mechanical characteristics.

4.2. Optimization of RB Process

4.2.1. One-Factor-at-a-Time Study

The effect of each of the three governing factors of the RB process on the roughness and surface microhardness was studied. The objects of study were the two integral height roughness parameters R_a and R_q , as well as the two shape roughness parameters, the skewness R_{sk} and kurtosis R_{ku} . The average initial roughness (after turning) was $R_a^{init} = 0.479 \mu\text{m}$. The influence of the radius r is illustrated in Figure 11a. The radius values in the range of 2 to 5 mm provide an integral height parameter R_a under $0.17 \mu\text{m}$, a kurtosis R_{ku} close to 3, and a negative skewness R_{sk} . Radii of 1 mm and 6 mm were excluded in further studies. Figure 11b visualizes the effect of burnishing force on the five selected surface texture characteristics. The integral height roughness parameters R_a and R_q decrease when the burnishing force increases (albeit weakly), while the skewness increases but remains negative. The kurtosis takes a value greater than 4 for a burning force in the interval 200–500 N. As expected, microhardness shows a tendency to increase with burnishing force. Figure 11c depicts the effect of the feed rate on the five investigated surface texture characteristics, of which R_a and R_q increase with the feed rate. This effect is more pronounced for R_q when the kurtosis trend is decreasing. The skewness remains negative, showing minimum values in the middle of the feed rate interval.

Compared with the height roughness parameters, the microhardness is less strongly affected by the radius (Figure 11a) and the burnishing force (Figure 11b). A minimum feed rate ensures

maximum surface microhardness and a steady trend of decreasing microhardness with increasing feed rate is observed. A possible explanation is the cyclic loading in the vicinity of each point of the processed surface due to the presence of the so-called overlapping effect [26]. The smaller the feed rate compared with the radius, the stronger this effect becomes. However, some of the observed trends may change if the values of the fixed factors in the one-factor-at-a-time experiment are altered. Therefore, a planned experiment is necessary.

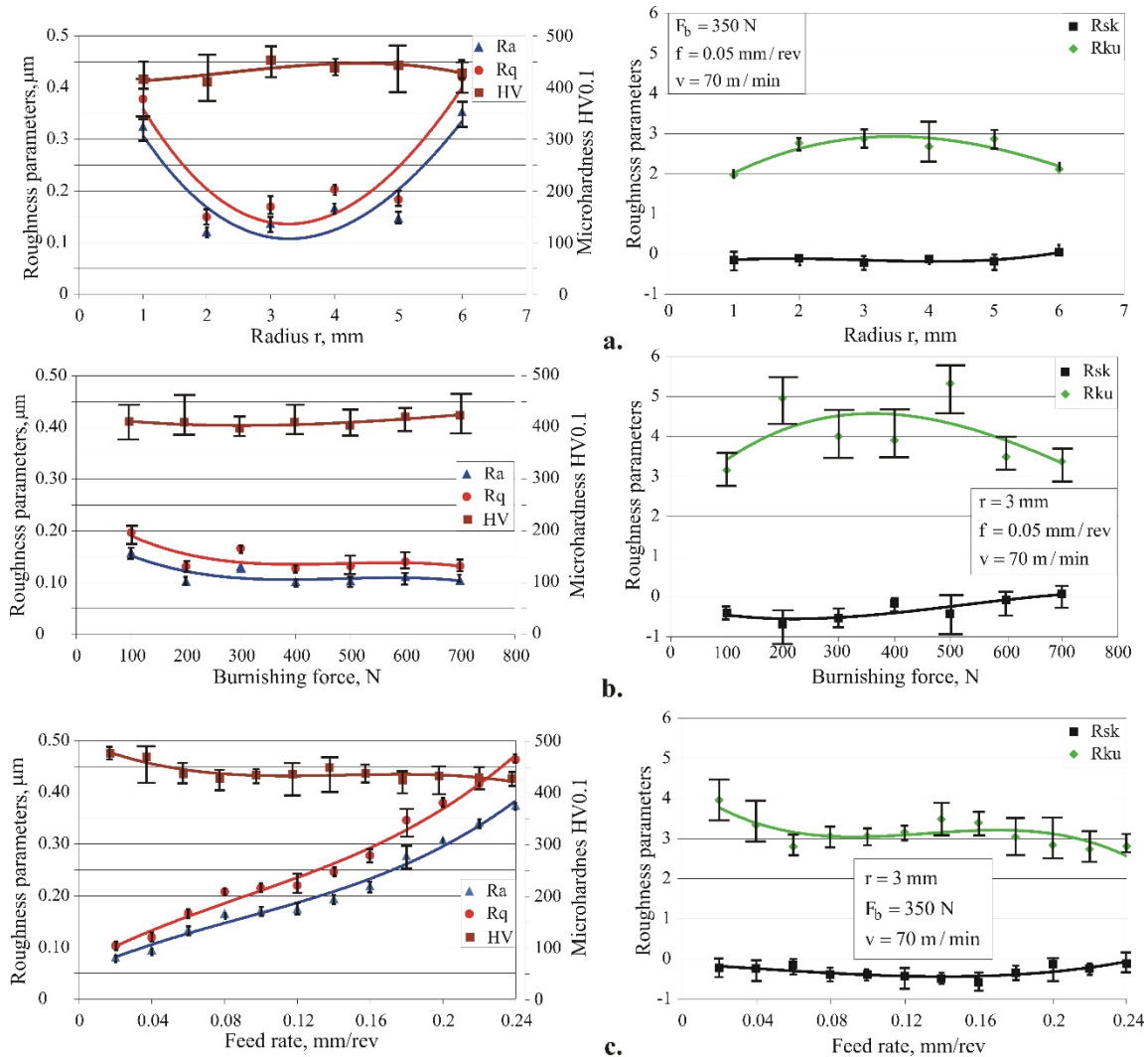


Figure 11. Influence of the radius (a), burnishing force (b) and feed rate (c) on the roughness height and shape parameters, and surface microhardness.

4.2.2. Planned Experiment

The levels of the governing factors are based on the outcomes of the one-factor-at-a-time study and are listed in Table 3. The dependence between the governing factors in natural \tilde{x}_i and coded x_i form is

$$x_i = \frac{2(\tilde{x}_i - \tilde{x}_{0,i})}{\tilde{x}_{\max,i} - \tilde{x}_{\min,i}}. \quad (17)$$

where $\tilde{x}_{\max,i}$, $\tilde{x}_{0,i}$, and $\tilde{x}_{\min,i}$ are the upper, middle, and lower levels of the i -th factor in natural coordinates, respectively.

Table 3. Levels of the governing factors.

Governing factors	Natural	Codded	Levels									
Radius of the roller toroidal surface	r , mm	x_1	2	3	3.5	4	5	-1	-0.333	0	0.333	1
Burnishing force	F_b , N	x_2	100	250	400	550	700	-1	-0.5	0	0.5	1
Feed rate	f , mm/rev	x_3	0.02	0.05	0.08	0.11	0.14					

The objective functions are the integral height roughness parameter Y_{R_a} and the surface microhardness Y_{HV} selected based on the results from the one-factor-at-a-time study. Given the wide ranges of variation of the governing factors (Table 3), a fourth-order central composition plan was chosen for the planned experiment. Table 4 lists the experimental outcomes from the planned experiment.

Table 4. Experimental plan and outcomes.

№	x_1	x_2	x_3	R_a , μm	R_a , μm scattering		Y_{R_a} , μm	HV	HV scattering		Y_{HV}
					+	-			+	-	
1	-1	-1	-1	0.133	0.014	0.008	0.1395	397.6	26	24	392.11
2	1	-1	-1	0.158	0.006	0.003	0.1624	402	32	21	400.23
3	-1	1	-1	0.107	0.014	0.026	0.1194	406.6	20	29	406.13
4	1	1	-1	0.261	0.022	0.015	0.2454	416.1	19	16	414.26
5	-1	-1	1	0.280	0.006	0.011	0.2783	397.1	29	30	400.23
6	1	-1	1	0.254	0.008	0.007	0.2554	388.0	27	29	392.11
7	-1	1	1	0.347	0.018	0.041	0.3614	413.9	20	32	414.26
8	1	1	1	0.236	0.048	0.019	0.2353	404.2	17	25	406.13
9	-1	0	0	0.245	0.012	0.013	0.2404	437.9	21	33	438.60
10	1	0	0	0.269	0.030	0.032	0.2404	439.3	35	34	438.60
11	0	-1	0	0.180	0.003	0.006	0.1559	390.4	17	24	390.40
12	0	1	0	0.147	0.006	0.008	0.1229	427.2	18	32	427.20
13	0	0	-1	0.270	0.033	0.038	0.2459	404.2	13	13	403.60
14	0	0	1	0.210	0.015	0.005	0.1859	403	24	22	403.60
15	-0.333	-0.5	-0.5	0.106	0.005	0.005	0.1428	400.4	16	33	406.20
16	0.333	-0.5	-0.5	0.141	0.011	0.012	0.1509	403.7	25	26	406.35
17	-0.333	0.5	-0.5	0.230	0.016	0.015	0.2057	420	22	44	444.72
18	0.333	0.5	-0.5	0.168	0.011	0.015	0.2224	436.1	26	28	444.87
19	-0.333	-0.5	0.5	0.144	0.008	0.004	0.1654	400.3	36	25	406.35
20	0.333	-0.5	0.5	0.171	0.028	0.011	0.1572	420.7	14	18	406.20
21	-0.333	0.5	0.5	0.214	0.031	0.020	0.2369	457.1	29	30	444.72
22	0.333	0.5	0.5	0.219	0.025	0.023	0.2202	466	14	25	444.87

Analysis of variance (ANOVA) was carried out using QStatLab [27] to study the significance of the governing factors. The ANOVA main effects are shown in Figure 12. The burnishing force (x_2) exerts the strongest influence on the roughness parameter R_a (Figure 12a) and the surface microhardness HV0.1 (Figure 12b). The second most important factor is feed rate (x_3). The influence

of the radius (x_1) is the weakest. The minimum value of R_a is obtained when all three governing factors are simultaneously maintained at the second level: $x_1 = -0.333$ and $x_2 = x_3 = -0.5$. The maximum microhardness is obtained when the three governing factors simultaneously occupy the fourth level: $x_1 = 0.333$ and $x_2 = x_3 = 0.5$.

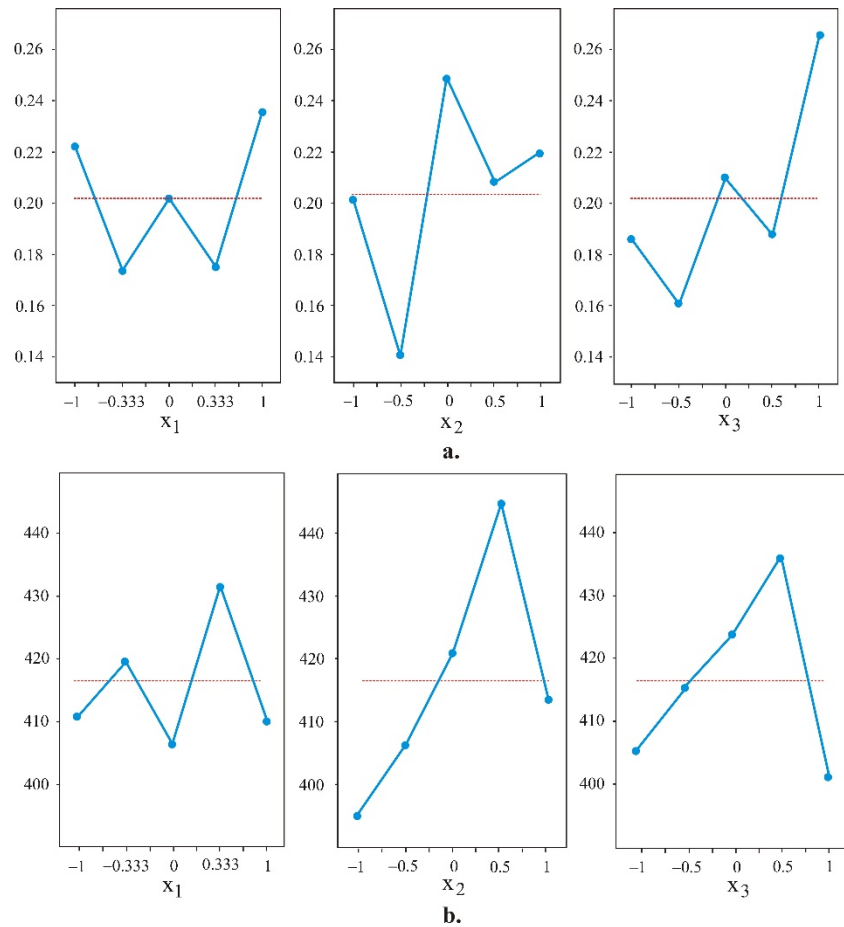


Figure 12. ANOVA main effects: a. roughness parameter R_a , μm ; b. microhardness HV0.1.

Regression analyses were conducted using QStatLab. The approximating polynomials were of order no higher than four, i.e. with one lower than the number of levels of the governing factors:

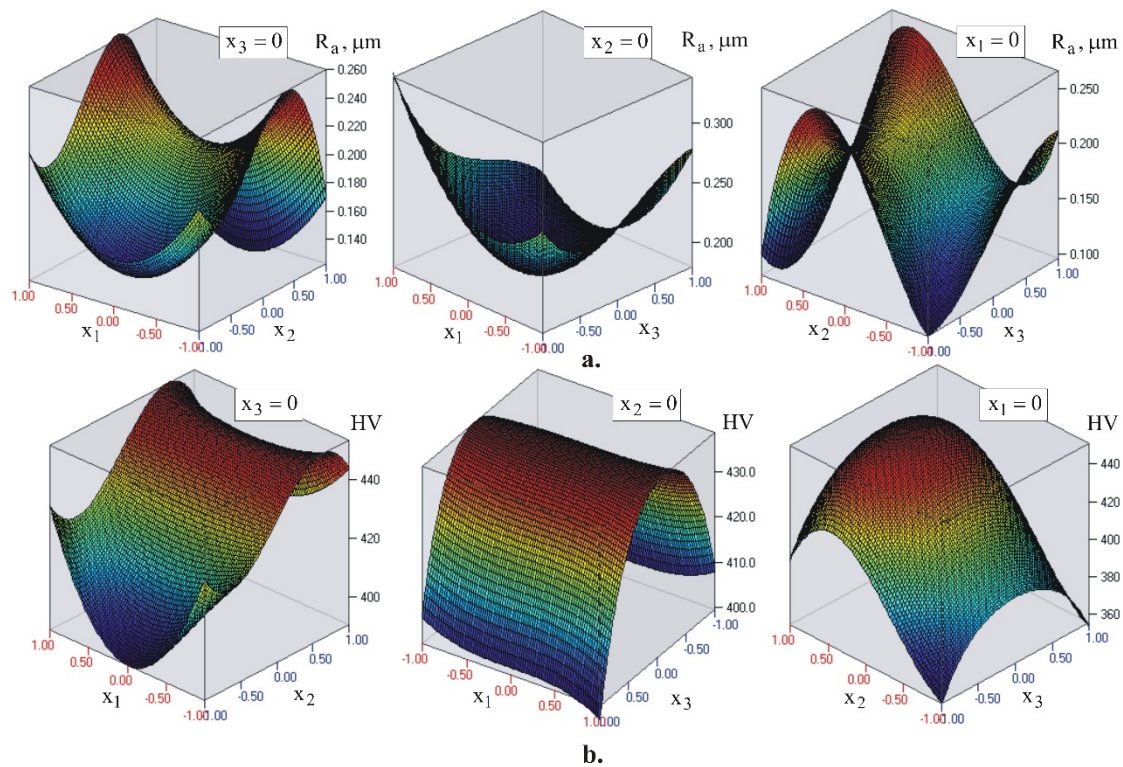
$$Y_k(\{X\}) = b_0 + \sum_{i=1}^m b_i x_i + \sum_{i=1}^{m-1} \sum_{j=i+1}^m b_{ij} x_i x_j + \sum_{i=1}^m b_{ii} x_i^2 + \dots, \quad k = 1, 2, \dots, q, \dots \quad (18)$$

where $\{X\}$ is the vector of the governing factors, m is the number of governing factors, and q is the number of objective functions.

Table 5 lists the coefficients of regression. A graphical visualization of the models is shown in Figure 13. The models confirm the conclusions drawn based on ANOVA regarding the influence of the governing factors on the roughness parameter R_a and the microhardness. The magnitudes of the objective functions calculated with (18) for the experimental design points are shown in Table 4. The comparison with the experimental results shows good agreement.

Table 5. Regression coefficients.

	b_0	b_2	b_{11}	b_{22}	b_{33}	b_{222}	b_{333}	b_{3333}
Y_{R_a}	0.185544	0.084417	0.054893	–	0.030350	–	–	0
Y_{HV}	438.6000	46.9170	0	–29.8000	–22.6117	–28,5170	0	–
								12.3883
	b_{13}	b_{112}	b_{123}	b_{223}	b_{233}	b_{1113}	b_{1122}	
Y_{R_a}	–	0	–	0.087953	0.032250	0	0	
Y_{HV}	0	–11.3875	0	0	0	–4.0633	29.3875	

Figure 13. Graphical visualization of the models: a. roughness parameter R_a ; b. microhardness.

4.2.3. Optimization

The three processes that can be implemented with the RB method are smoothing, hardening, and mixed RB. The first of these achieves a minimum value of the integral height parameter R_a . The goal of the second process is to maximize the surface microhardness. Mixed RB achieves compromise values of R_a and the surface microhardness. Finding the optimal values of the governing factors for the first two processes requires solving single-objective optimization problems, i.e., finding the minimum value of the objective function Y_{R_a} , respectively finding the maximum value of the objective function Y_{HV} , whereby the governing factors are varied in the defined factor space. However, the radius changes discretely and takes values according to Table 3. Therefore, instead of minimizing or maximizing the Y_{R_a} or Y_{HV} value, respectively, another approach was applied. Based on ANOVA, points 15 and 22 were selected from the experiment plan, for which the magnitudes of the governing parameters provide minimum roughness and maximum microhardness, respectively. These combinations of governing factors are only compromise optimal rather than optimal. A multi-objective optimization problem needs to be solved to realize a mixed RB

process: $Y_{R_a} \rightarrow \min$ and $Y_{HV} \rightarrow \max$ with the constraints on the governing factors shown in Table 3. The following functional constraints are also defined: $R_a < 0.2 \mu\text{m}$ and $HV > 410$. The decision was made with the nondominated sorting genetic algorithm [28] using QstatLab. The compromise optimal solution was selected from the Pareto front. Figure 14 illustrates the Pareto front and the chosen compromise optimal solution. Table 6 provides detailed information regarding the solution results for the three optimization tasks.

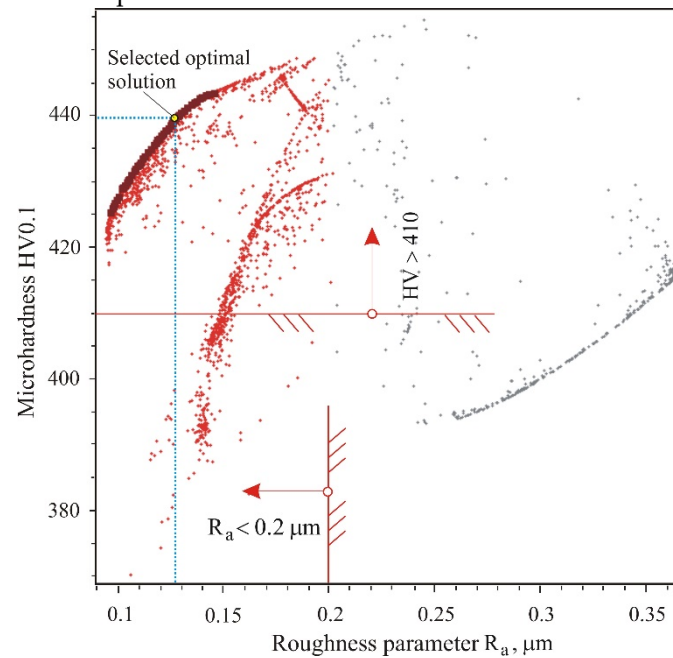


Figure 14. Generated Pareto front.

Table 6. Compromise optimal values.

Process	x_1^*	r^* , mm	x_2^*	F_b^* , N	x_3^*	f^* , mm/rev	R_a^* , μm	HV^*
Smoothing	-0.333	3	-0.5	250	-0.5	0.05	0.106	400.4
Hardening	0.333	4	0.5	550	0.5	0.11	0.219	466
Mixed	-1	2	1	700	0.4212	0.0547	0.127	439.1

4.3. SRB Investigation

4.3.1. Formulation of the Study

As a result of the RB optimization, the optimal values of the governing factors for three RB processes smoothing, hardening, and mixed, were obtained (see Table 6). Using the governing factors of each of the three processes, SRB was implemented with different values of the crossing angle α . The specimens had the same shape and dimensions as those used for the RB research and optimization (see Figure 9). The subject of the research is the variation of the roughness parameter R_a and surface microhardness HV0.1 as a function of the crossing angle α . When $\alpha = 0^\circ$, the RB process is implemented and the obtained results for R_a and HV0.1 represent an experimental verification of the results obtained from the optimizations in Section 4.2.3. For each of the three RB processes (smoothing, hardening, and mixed), the optimal values of the governing factors are used to implement SRB and an optimal value of α is selected.

4.3.2. Effect of Crossing Angle on the Roughness Parameter R_a and Microhardness

The effect of the crossing angle on the roughness parameter R_a and surface microhardness HV0.1 is illustrated in Figure 15. For all values of α (except for two experimental points in Figure 15c), SRB achieves a significantly lower roughness parameter R_a compared with the RB process, i.e., when $\alpha = 0^\circ$. The largest reduction, by more than a factor of two, was obtained for the hardening process. Since there is a positive correlation between the roughness height parameters R_a and R_z , the experimental results obtained for R_a confirm the theoretical justifications in Section 2.4 for a smaller kinematic roughness in the SRB process.

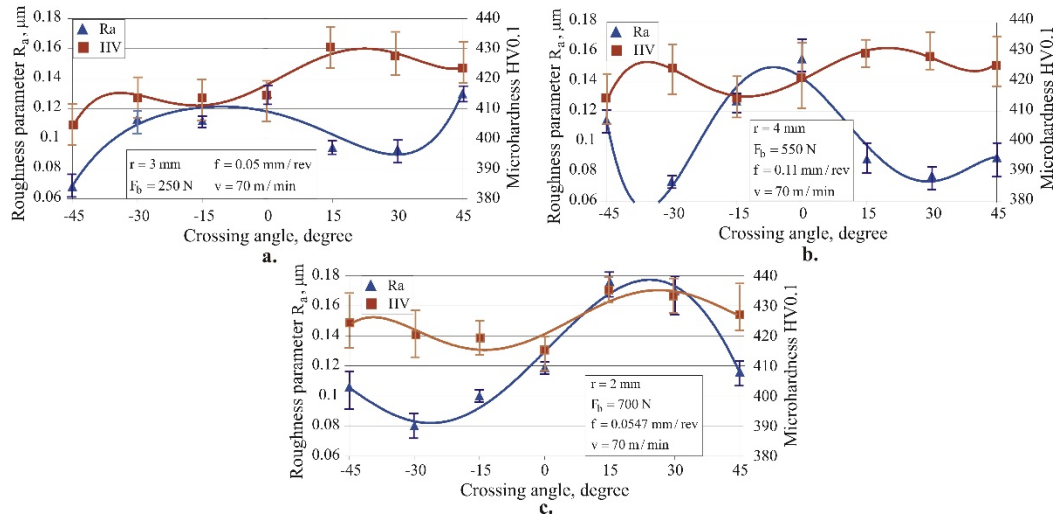


Figure 15. Effect of crossing angle on roughness parameter R_a and microhardness HV0.1: a. smoothing, b. hardening, c. mixed processes.

For all α values (except for one experimental point in Figure 15a and two points in Figure 15b), SRB increases the surface microhardness HV0.1. This is due to the greater equivalent plastic deformation of the surface layer, and hence greater strain hardening.

Based on the obtained results for R_a and HV0.1 (Figure 15), the following values of the crossing angle α were selected for the three processes: for smoothing SRB, $\alpha = -45^\circ$ (Figure 15a), since the main objective is to minimize the height roughness parameters, and for hardening and mixed SRB processes, $\alpha = -30^\circ$ (Figure 15b and Figure 15c), since high microhardness is combined with the inherent main advantage of SRB, namely lower roughness. From this point of view, the identification of smoothing, hardening, and mixed SRB processes is conditional.

4.4. Effect of RB and SRB on Surface Integrity: Comparative Analysis

4.4.1. Formulation of the Study

Two samples were selected for each of the three processes (see Figure 15). One was treated with RB ($\alpha = 0^\circ$) and the other with SRB with the crossing angle values chosen in Section 4.3.2. A comparison of the surface integrity characteristics (roughness parameters, microhardness HV0.1, and residual axial and hoop stress distributions) was performed for each pair of samples.

4.4.2. Smoothing Process

A comparison of the 2D roughness parameters and surface microhardness obtained via smoothing RB and SRB processes is shown in Table 7. The height roughness parameters obtained via smoothing SRB demonstrate the great potential of this process for minimizing roughness. The integral height parameters R_a and R_q are reduced by a factor of approximately two, while the

local height parameters R_p and R_v , as well as the family of functional parameters R_k , are reduced by an even greater factor. Significantly lower values of height roughness parameters after SRB are a prerequisite for reducing friction [29], and improving fatigue behavior [30,31] and corrosion resistance [32], compared with RB. The shape parameters, skewness R_{sk} and kurtosis R_{ku} , are important indicators of tribological behavior because they characterize the distribution and shapes of peaks and valleys. It is known that a surface texture characterized by a negative skewness ($R_{sk} < 0$) and a higher kurtosis (>3) improves lubrication and reduces friction [23,33]. This effect is mainly due to the dominance of deep valleys when $R_{sk} < 0$. These valleys act as micro-reservoirs that hold the lubricant. In this respect, the smoothing SRB process provides negative skewness and kurtosis with a value close to 3 (Table 7). Smoothing SRB leads to a slight reduction (by 2.4%) of the surface microhardness compared with smoothing RB (Table 7). A comparison of the evaluation profiles obtained via the smoothing RB and SRB processes is shown in Figure 16.

Table 7. Comparison of the surface integrity characteristics obtained via smoothing RB and SRB processes.

Process	Surface integrity characteristics									
	2D Roughness parameters									Microhardness
	R_a μm	R_q μm	R_p μm	R_v μm	R_{sk}	R_{ku}	R_k μm	R_{pk} μm	R_{vk} μm	HV0.1
RB	0.130	0.167	0.388	0.672	-0.569	4.348	0.416	0.146	0.231	414
SRB	0.068	0.083	0.182	0.245	-0.221	2.650	0.212	0.056	0.100	404

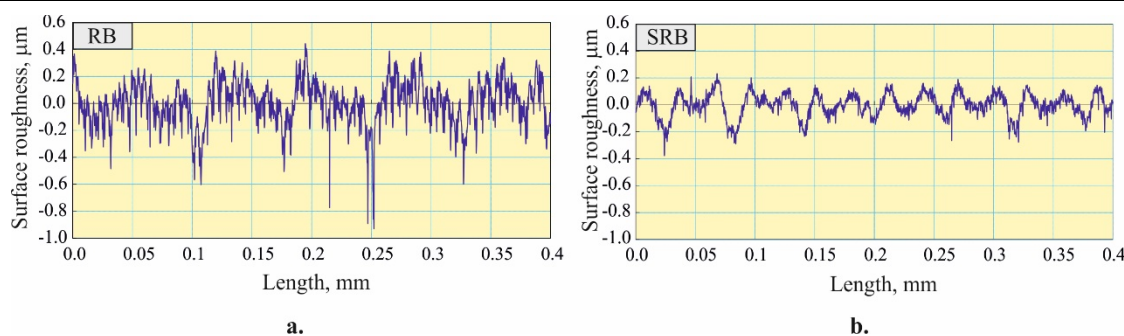


Figure 16. Evaluation profiles: a. RB and b. SRB smoothing processes.

Figure 17 illustrates the distribution of RS introduced by the RB and SRB smoothing processes. Both methods introduce significant compressive RS at depths greater than 0.5 mm. The axial RS introduced by RB in the surface layer and in subsurface layers up to a depth of 0.05 mm is greater in absolute value. In contrast, the SRB introduces larger absolute compressive hoop RS at a depth of up to 0.15 mm. Since both RSs slow down the formation and development of fatigue macro-cracks, it is difficult to predict which of the two smoothing processes is more effective at improving fatigue strength.

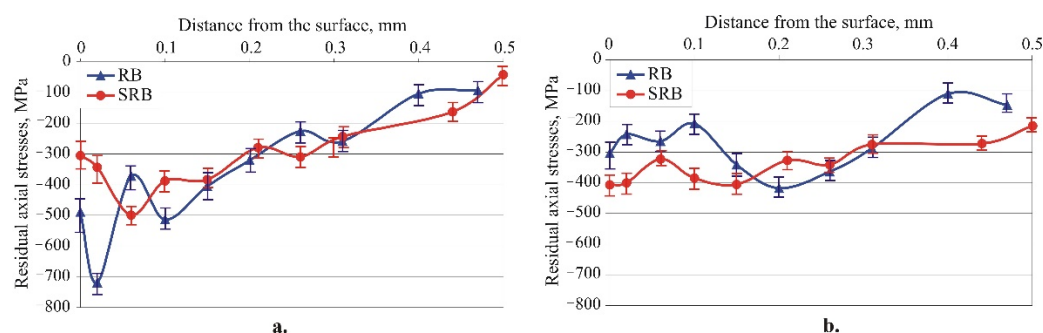


Figure 17. Residual stress distribution due to smoothing processes: a. axial; b. hoop.

4.4.3. Hardening Process

A comparison of the 2D roughness parameters and surface microhardness obtained via hardening RB and SRB processes is shown in Table 8. The larger equivalent plastic strain during hardening SRB provides two effects: a more favorable combination of shape roughness parameters from the point of view of improving tribological behavior in boundary and mixed friction conditions ($R_{sk} = -0.531$ and $R_{ku} = 5.04$), and a visible increase in microhardness relative to hardening RB.

Table 8. Comparison of the surface integrity characteristics obtained via hardening RB and SRB processes.

Process	Surface integrity characteristics									Microhardness HV0.1
	2D Roughness parameters									
	R_a μm	R_q μm	R_p μm	R_v μm	R_{sk}	R_{ku}	R_k μm	R_{pk} μm	R_{vk} μm	
RB	0.163	0.202	0.466	0.631	-0.248	3.417	0.555	0.153	0.223	421
SRB	0.073	0.093	0.225	0.420	-0.531	5.040	0.233	0.088	0.137	424

It is important to note that hardening SRB does not change the integral 2D height roughness parameters R_a and R_q significantly in comparison with smoothing SRB, and for the remaining 2D height roughness parameters, a slight deterioration is observed. This shows that the smoothing effect is highly pronounced for both smoothing and hardening SRB. The comparison of evaluation profiles obtained via hardening RB and SRB processes (Figure 18) confirms this advantage of SRB.

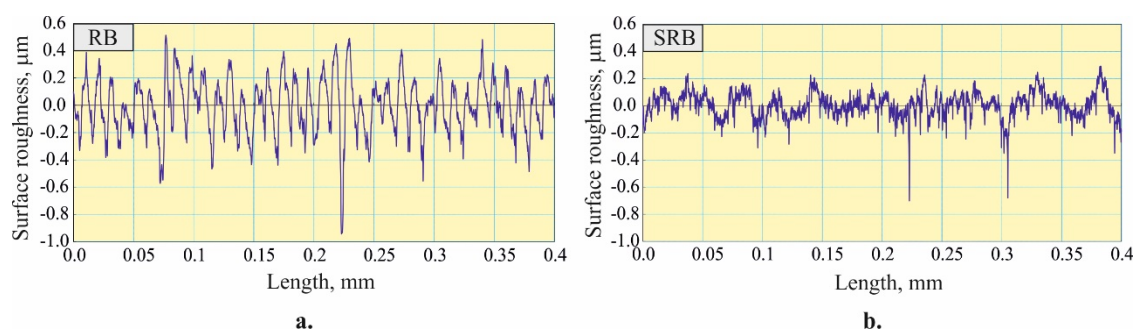


Figure 18. Evaluation profiles: a. RB and b. SRB hardening processes.

Summing up, all the surface integrity characteristics obtained via hardening SRB have improved values compared with hardening RB (Table 8). These results show the technological capabilities of hardening SRB to simultaneously provide favorable height and shape roughness parameters and surface microhardness. Therefore, the hardening SRB process can be used to significantly improve the tribological, fatigue, and corrosion behavior of AISI 316 steel components.

Figure 19 depicts the RS distribution due to the RB and SRB hardening processes. For both hardening processes, the depth of the compression zone is greater than 0.5 mm, for both axial and hoop RS. A comparison with Figure 17 shows that hardening processes provide a greater depth for the compressive zone. The larger equivalent plastic strain results in larger surface compressive RSs for both RB and SRB. RB introduces greater compressive axial RS at depths up to ≈ 0.09 mm, after which the trend changes in favor of SRB. Conversely, the SRB introduces larger compressive hoop RS into the surface and subsurface layers at depth ≈ 0.3 mm. Similar to the smoothing processes, it is difficult to predict based only on the RS distribution which of the two methods (RB or SRB) is more effective at enhancing fatigue strength.

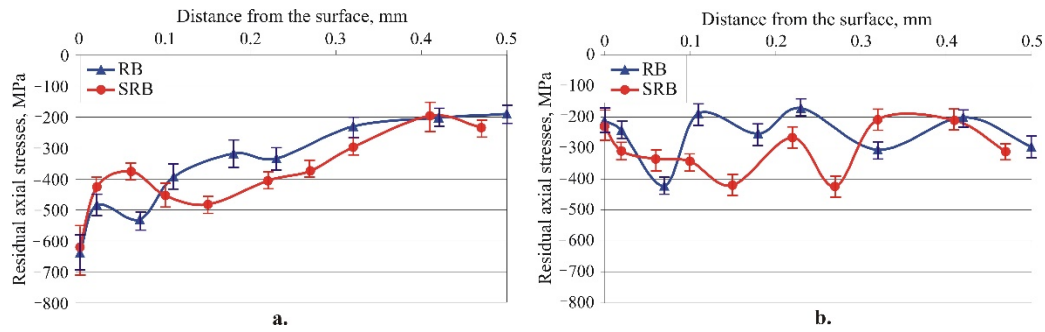


Figure 19. Residual stress distribution due to hardening processes: a. axial; b. hoop.

4.4.4. Mixed Process

Table 9 shows a comparison of the 2D roughness parameters and surface microhardness obtained via the mixed RB and SRB processes. The surface integrity characteristics after mixed SRB are close to those obtained after hardening SRB, with a slight deterioration of the R_a and R_q height roughness parameters. The same trends are observed as with hardening SRB, but mixed SRB provides a more favorable combination of shape roughness parameters: the skewness parameter is negative, but with a larger absolute value ($R_{sk} = -0.763$) and the kurtosis parameter is larger ($R_{ku} = 5.748$). The surface microhardness HV0.1 obtained via mixed SRB decreases slightly (by 4 units) relative to the hardening SRB. Therefore, the hardening and mixed SRB processes provide very similar surface integrity characteristics. A comparison of the evaluation profiles obtained via mixed RB and SRB processes is shown in Figure 20.

Table 9. Comparison of the surface integrity characteristics obtained via mixed RB and SRB processes.

Process	Surface integrity characteristics									
	2D Roughness parameters						Microhardness			
	R_a μm	R_q μm	R_p μm	R_v μm	R_{sk}	R_{ku}	R_k μm	R_{pk} μm	R_{vk} μm	HV0.1
RB	0.117	0.145	0.342	0.429	-0.274	2.907	0.381	0.122	0.172	415
SRB	0.080	0.105	0.217	0.441	-0.763	5.748	0.238	0.077	0.175	420

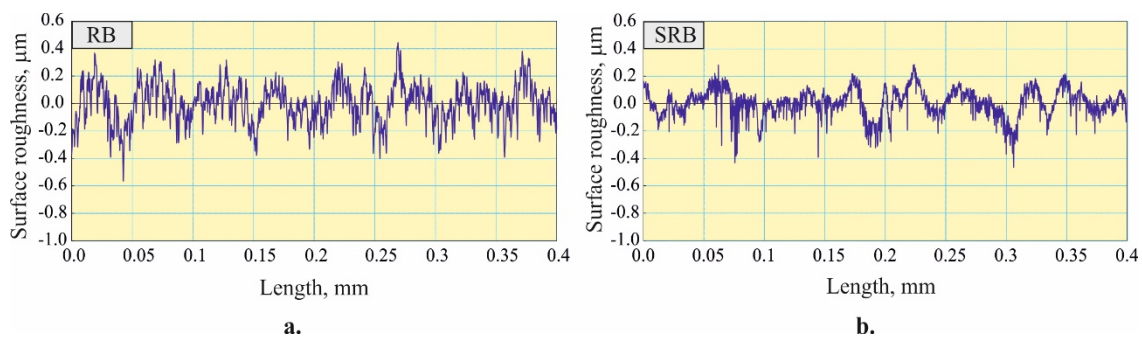


Figure 20. Evaluation profiles: a. RB and b. SRB mixed processes.

Figure 21 shows the distribution of RS introduced by the RB and SRB mixed processes. For both of these, the same trends are observed regarding the depth and intensity of the compressive zones, as in the case of hardening processes (see Figure 19). The experimental RS distributions obtained for the three processes (smoothing, hardening, and mixed) confirm the effectiveness of single-toroidal RB and SRB at introducing a deep zone with high compressive RS in AISI 316 steel components.

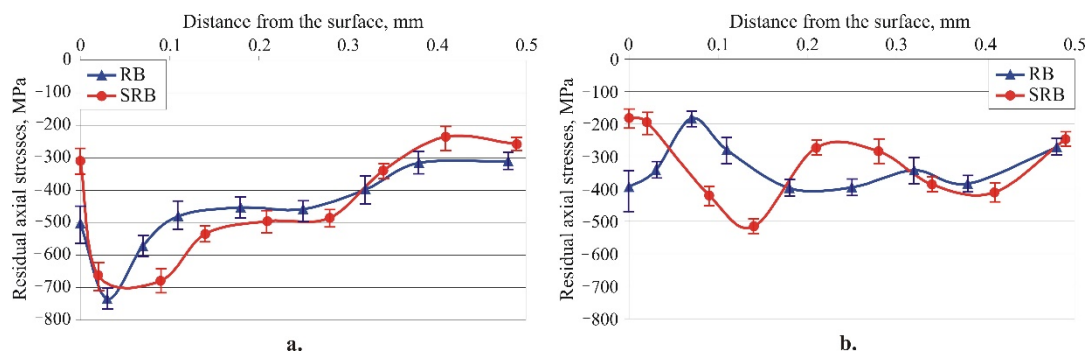


Figure 21. Residual stress distribution due to mixed processes: a. axial; b. hoop.

5. Conclusions

A new method called SRB and a multi-functional device for surface cold working of cylindrical outer surfaces have been developed. The deforming element is a toroidal roller whose axis crosses that of the workpiece. SRB is based on the well-known single-toroidal RB, in which the axes of the roll and the workpiece are parallel. The two methods were applied to cold working of AISI 316 steel outer cylindrical surfaces. The main advantage of the SRB is that it provides smaller height roughness parameters and a higher surface microhardness than RB. The major new findings are as follows:

The new method was investigated theoretically and experimentally. Based on the theoretical background of SRB, it was established that RB is a special case of SRB. Due to the crossing axes of the deforming roller and workpiece, a relative sliding velocity occurs in the contact zone between the roller and the machined surface. The direction of the sliding velocity vector depends on the size of the crossing angle and is set by the new burnishing device. This makes it possible to realize a desired surface texture. When the two axes are parallel, the well-known RB method is implemented. The relationship between the finishing and the surface integrity characteristics was investigated for both methods.

Three combinations of optimal sizes of RB governing factors were found, with which three processes were realized: smoothing, hardening and mixed. Using the same three combinations of governing factor sizes, the optimal crossing angle values for the SRB were found. The distinctions between smoothing, hardening and mixed processes were found to be largely irrelevant to SRB, as with all three combinations of governing factors, SRB achieved roughness and microhardness values within a narrow range. For instance, the roughness parameter R_a and microhardness HV0.1 remained within the ranges (0.068–0.080) μm and (404–424) HV0.1, respectively.

It was established that the implementation of the SRB process with a crossing angle of $\alpha = -30^\circ$ (for hardening and mixed) and $\alpha = -45^\circ$ (for smoothing) reduces the roughness parameter (0.068–0.080 μm) of AISI 316 steel samples by factor of about two compared to the basic smoothing, hardening, and mixed RB processes (0.117–0.163 μm). Therefore, the smoothing is a mandatory effect in SRB, regardless of the equivalent plastic strain degree. The minimization of all the height roughness parameters via SRB should significantly improve the fatigue life and corrosion resistance of the components.

Both the RB and SRB processes provide a favorable surface texture characterized by negative skewness and a kurtosis close to or greater than three. This effect is more pronounced in SRB than in RB, when the strain hardening is greater. Therefore, SRB implemented as a hardening or mixed processes is particularly suitable for improving the tribological behavior of AISI 316 steel components under boundary and mixed friction conditions.

Single-toroidal RB and SRB (for all three implementation options: smoothing, hardening, and mixed processes) introduce significant compressive RS at a depth greater than 0.5 mm. However, on the basis of only RS distribution, it is not possible to predict which of the two methods is more effective at enhancing fatigue strength.

Both single-toroidal RB and SRB provide substantial improvement in the investigated surface integrity characteristics, but SRB has a significant advantage in terms of roughness and

microhardness. On the basis of only roughness, microhardness, and RS distribution, it is difficult to predict the operational behavior (wear under dry friction conditions and fatigue) of machined components, since the microstructure and orientation of the surface texture are important surface integrity characteristics. Therefore, to establish which of the two methods provides better operational behavior, additional studies of the relationships between the surface integrity characteristics and the wear resistance and fatigue behavior are necessary.

Author Contributions: Conceptualization, J.M. and G.D.; methodology, J.M. and G.D.; software, J.M. and G.D.; validation, J.M., G.D., A.A. and V.D.; formal analysis, G.D. and J.M.; investigation, A.A., V.D., K.A., P.D., G.D., and J.M.; resources, J.M. and G.D.; data curation, J.M. and G.D.; writing—original draft preparation, J.M. and G.D.; writing—review and editing, J.M. and G.D.; visualization, J.M., G.D., A.A., and V.D.; supervision, J.M. and G.D.; project administration, J.M. and G.D.; funding acquisition, J.M. and G.D. All authors have read and agreed to the published version of the manuscript.

Funding: This research was supported by the European Regional Development Fund within the OP. “Science and Education for Smart Growth 2014–2020”, Project CoC “Smart Mechatronics, Eco- and. Energy Saving Systems and Technologies”, No.BG05M2OP001-1.002-0023.

Data Availability Statement: Not applicable.

Conflicts of Interest: “The authors declare no conflict of interest.”.

References

1. Ecoroll Catalogue. Tools and Solutions for Metal Surface Improvement; Ecoroll Corporation Tool Technology: Milford, OH, USA, 2006
2. Korzynski, M. Slide diamond burnishing. In: Korzynski M (ed) Nonconventional finishing technologies. Polish Scientific Publishers, Warsaw, **2013**, pp 9–33
3. Dwivedi, D.K. Surface Engineering. In *Enhancing Life of Tribological Components*; Springer: New Delhi, India, **2018**; ISBN 978-81-322-3779-2.
4. Korzynski, M. Modelling and experimental validation of the force-surface roughness relation for smoothing burnishing with a spherical tool. *Int J Mach Tool Manuf*, **2007**, *47*(12), 1956-1964.
5. Maximov, J.T.; Duncheva, G.V.; Anchev, A.P.; Dunchev, V.P. Slide burnishing versus deep rolling – a comparative analysis. *Int J Adv Manuf Technol*, **2020**, *110*, 1923-1939.
6. Maximov, J.T.; Duncheva, G.V.; Anchev, A.P.; Dunchev, V.P.; Argirov, Y.B. Effect of Diamond Burnishing on Fatigue Behaviour of AISI 304 Chromium-Nickel Austenitic Stainless Steel. *Materials*. **2022**; *15*(14):4768.
7. Prevey, P.S. Burnishing method and apparatus for providing a layer of compressive residual stress in the surface of a workpiece. USA Patent 5826453 [patented October 27, 1998]
8. Prevey, P.S. The effect of cold work on the thermal stability of residual compression in surface enhanced IN718. Proceedings: 20th ASM Materials Solutions Conference & Exposition St. Louis, Missouri, October 10-12, 2000.
9. Prevey, P.S.; Ravindranath, R.; Shepard, M.; Gabb, T. Case Studies of Fatigue Life Improvement Using Low Plasticity Burnishing in Gas Turbine Engine Applications. Presented June 2003 at the ASME Turbo Expo. Atlanta, GA.
10. Balevski, A.T. Metal Science; Technika: Sofia, Bulgaria, **1988**. (In Bulgarian)
11. Tugay, I.O.; Hosseinzadeh, A.; Yapici, G.G. Hardness and wear resistance of roller burnished 316L stainless steel. *Materials Today: Proceedings*, **2021**, *47*, 2405-2409.
12. Akkurt, A. Comparison of roller burnishing method with other hole surface finishing processes applied on AISI 304 austenitic stainless steel. *J Mater Eng Perform*, **2011**, *20*(6), 960-968.
13. Gharbi, K.; Ben Moussa, N.; Ben Rhouma, A.; Ben Fredj, N. Improvement of the corrosion behavior of AISI 304L stainless steel by deep rolling treatment under cryogenic cooling. *Int J Adv Manuf Technol*, **2021**, *117*, 3841–3857.
14. Juijerm, P.; Altenberg, I. Fatigue performance enhancement of steels using mechanical surface treatments. *Journal of Metals, Materials and Minerals*, **2007**, *17*(1), 59-65.
15. Juijerm, P.; Altenberg, I. Fatigue performance of high-temperature deep-rolled metallic materials. *Journal of Metals, Materials and Minerals*, **2007**, *17*(2), 37-41.
16. Munoz-Cubillos, J.; Coronado, J.J.; Rodriguez, S.A. Deep rolling effect on fatigue behaviour of austenitic stainless steels. *Int J Fatigue*, **2017**, *95*, 120-131.
17. Nikitin, I.; Altenberger, I.; Scholtes, B. Effects of deep rolling at elevated and low temperatures on the isothermal fatigue of AISI304. *Alternative Processes*. **2005**, *70*, 185–190.

18. Nikitin, I.; Altenberger, I. Comparison of the fatigue behaviour and residual stress stability of laser-shock peened and deep rolled austenitic stainless steel AISI 304 in the temperature range 25–600°C. *Mater Sci Eng A*, **2007**, *465*, 176-182.
19. Nikitin, I.; Scholtes, B.; Maier, H.J.; Altenberger, I. High temperature fatigue behaviour and residual stress stability of laser-shock peened and deep rolled austenitic steel AISI 304. *Scripta Materialia*, **2004**, *50*, 1345-1350.
20. Tadi, A.J.; Hosseini, S.R.; Semiromi, N.M. Formation of surface nano/ultrafine structure using deep rolling process on the AISI 316L stainless steel. *Material Sci & Eng Int J*, **2017**, *1(3)*, 88-93.
21. Yilmaz, H.; Sadeler, R. Impact wear behaviour of ball burnished 316L stainless steel. *Surf Coat Technol*, **2019**, *363*, 369-378.
22. Korzynski, M.; Dudek, K.; Korzynska, K. Effect of slide diamond burnishing on the surface layer of valve stems and the durability of the stem-graphite seal friction pair. *Applied Sciences*, **2023**, *13*, 6392.
23. Korzynski, M.; Dudek, K.; Kruczek, B.; Kocurek, P. Equilibrium surface texture of valve stems and burnishing method to obtain it. *Tribol Int*, **2018**, *124*, 195-199.
24. Korzynski, M.; Dudek, K.; Palczak, A.; Kruczek, B.; Kocurek P. Experimental models and correlations between surface parameters after slide diamond burnishing. *Measurement Science Review*, **2018**, *18(3)*, 123-129.
25. Skoczylas, A.; Zaleski, K.; Matuszal, J.; Ciecielag, K.; Zaleski, R.; Gorgol, M. Influence of slide burnishing parameters on the surface layer properties of stainless steel and mean positron lifetime. *Materials*, **2022**, *15*, 8131.
26. Maximov, J.T.; Duncheva, G.V.; Anchev, A.P.; Ganev, N.; Dunchev, V.P. Effect of cyclic hardening on fatigue performance of slide burnishing components made of low-alloy medium carbon steel. *Fatigue Fract Eng Mater Struct*, **2019**, *42(6)*, 1414-1425.
27. Vuchkov, I.N.; Vuchkov, I.I. *QStatLab Professional*, version 6.1.1.3; Statistical Quality Control Software, User's Manual; QStatLab: Sofia, Bulgaria, 2009.
28. Deb, K.; Pratap, A.; Agarwal, S.; Meyarivan T. A fast and elitist multiobjective genetic algorithm: NSGA-II. *IEEE Transactions on Evolutionary Computation* **2002**, *6(2)*, 182-197.
29. Pawlus, P.; Reizer, R.; Wieczorowski, M. Functional Importance of Surface Texture Parameters. *Materials* **2021**, *14*, 5326.
30. Alang, N.A.; Razak, N.A.; Miskam, A.K. Effect of Surface Roughness on Fatigue Life of Notched Carbon Steel. *Int. J. Eng. Technol. IJET-IJENS* **2011**, *11*, 161–163.
31. Li, C.; Dai, W.; Duan, F.; Zhang, Y.; He, D. Fatigue Life Estimation of Medium-Carbon Steel with Different Surface Roughness. *Appl. Sci.* **2017**, *7*, 338.
32. Whitehouse, D.J. *Handbook of Surface and Nanometrology*; CRC Press: Boca Raton, FL, USA, 2011.
33. Sedlacek, M.; Podgornik, B.; Vizintin, J. Correlation between standard roughness parameters skewness and kurtosis and tribological behavior of contact surface. *Tribology International* **2012**, *48*, 102-112.

Disclaimer/Publisher's Note: The statements, opinions and data contained in all publications are solely those of the individual author(s) and contributor(s) and not of MDPI and/or the editor(s). MDPI and/or the editor(s) disclaim responsibility for any injury to people or property resulting from any ideas, methods, instructions or products referred to in the content.